sustainability

MDPI

Article

Carbon Deposition Characteristics in Thermal Conversion of Methane for Sustainable Fuel

Xiaorong Zhang [1], Jie Wang [2], Zhanlong Song [1,*] and Yingping Pang [1]

[1] National Engineering Laboratory for Reducing Emissions from Coal Combustion, Engineering Research Center of Environmental Thermal Technology of Ministry of Education, Shandong Key Laboratory of Energy Carbon Reduction and Resource Utilization, School of Energy and Power Engineering, Shandong University, Jinan 250061, China; zhangxr1216@126.com (X.Z.); yppang@sdu.edu.cn (Y.P.)

[2] College of Chemical Engineering, Shanxi Institute of Science and Technology, Jincheng 048000, China; wangjie2@sxist.edu.cn

* Correspondence: zlsong@sdu.edu.cn; Tel.: +86-0531-88399372

Abstract: Low-carbon powertrains and sustainable fuels are closely linked as they both aim to reduce carbon emissions and transition away from reliance on fossil fuels. The methane from biogas, biomass, and organic waste can serve as an alternative energy source to traditional fossil fuels. The process of obtaining sustainable fuel (e.g., hydrogen and syngas) from methane is commonly confronted with the problems of carbon deposition on metal oxide. The study of carbon deposition characteristics during methane thermal conversion processes is particularly crucial for low-carbon powertrains. Herein, the carbon deposition on $CoAl_2O_4$ and strongly alkali-etched $CoAl_2O_4$ ($CoAl^vO_4$) spinel oxides from the CH_4 stage was investigated. We demonstrate that reaction time, calcination temperature, and reaction temperature have no effect on the compositions of carbon deposition, and the material itself plays a crucial role in carbon deposition. The graphitization degree for $CoAl^vO_4$ is lower than that for $CoAl_2O_4$. The strong alkali etching in $CoAl_2O_4$ only affects contents in different composition carbon deposition. This is mainly attributed to the introduction of Al^{3+} vacancies by alkali etching, which efficiently tunes the surface electronic structure in $CoAl_2O_4$. These findings guide designing efficient and clean low-carbon powertrains, especially in the development of removal carbon deposition technologies and catalysts.

Keywords: carbon deposition; Co-Al spinel oxides; strong alkali etching; CH_4 conversion; sustainable fuels

check for updates

Citation: Zhang, X.; Wang, J.; Song, Z.; Pang, Y. Carbon Deposition Characteristics in Thermal Conversion of Methane for Sustainable Fuel. *Sustainability* **2024**, *16*, 5035. https://doi.org/10.3390/su16125035

Academic Editors: Hongliang Luo, Weidi Huang and Gengxin Zhang

Received: 7 May 2024
Revised: 3 June 2024
Accepted: 12 June 2024
Published: 13 June 2024

1. Introduction

Low-carbon powertrains are essential for sustainable development and minimizing carbon emissions [1], which play a pivotal role in shaping a more environmentally conscious future. The utilization of sustainable fuels represents a significant step towards enhancing eco-friendliness and operational efficiency across various sectors [2]. The transition to sustainable fuels not only supports the shift towards low-carbon powertrains but also contributes to global endeavors aimed at achieving climate goals through the substantial reduction in greenhouse gas emissions originating from conventional fossil fuels [3]. The energy demand is expected to be met largely by sustainable energy and natural gas [4,5].

Methane derived from biogas, biomass, and organic waste [6], along with sustainable fuels such as hydrogen and syngas extracted from methane, are increasingly being adopted across diverse industries, signaling a paradigm shift towards a more sustainable and environmentally responsible energy landscape. Hydrogen is widely recognized as a sustainable and clean energy carrier, prized for its high energy density and emission of only water upon utilization [7,8]. Meanwhile, syngas serves as a crucial chemical intermediate, playing an indispensable role across various industries. It can be transformed into high-value-added

products such as alcohols and aldehydes, as well as fuels including olefins, waxes, and diesel, among others [9,10].

The methane thermal conversion process is commonly confronted with the problems of carbon deposition on metal oxide due to the reaction of methane decomposition (1). Carbon formation over solid catalysts is mainly due to the metal-catalyzed decomposition of these feedstocks at high temperatures [11] and involves hydrogen transfer, dehydrogenation, and polycondensation steps [12]. As a non-desorbed product, carbon is located in the pores and on the external surface, thus covering active sites and blocking pores, resulting in catalyst deactivation [12–14]. Noble metal catalysts show excellent activities with minimal carbon deposition. However, they have limited application value of sustainable practices due to their high cost and low abundance [15]. As an alternative, spinel oxides containing Co element are known for high methane conversion ability due to the high oxygen equilibrium partial pressure of Co [16,17]; however, the deactivation catalysts due to carbon deposition still pose challenges for industrialization [18].

$$CH_4 \rightarrow C + 2H_2 \quad \text{(R1)}$$

The effective regeneration of catalysts is critical for sustainable development, thus achieving the stability of catalysts after repeated reaction–regeneration cycles. Therefore, the elimination of carbon deposition is necessary to restore catalyst activity and to ensure continuous operation in industrial processes. Currently, the commonly used methods for eliminating carbon deposits include using oxidation in Air/O_2, gasification in CO_2/H_2O, and so on [12,14,19,20]. The elimination of carbon with air combustion is often the preferred and most practical route. However, this process produces a large amount of carbon dioxide (CO_2) emissions [12,21], and high exothermicity can easily cause overheating, leading to metal sintering and catalyst deactivation.

To meet the concept of "green carbon science" and make full use of carbon deposition, carbon can be significantly eliminated by gasification using H_2O and CO_2. Synthesis gas, instead of CO_2, is the main product in these processes [22]. Compared to steam gasification, CO_2 gasification has several advantages. Unlike steam, CO_2 is a gas and thus requires no vaporization before gasification. CO_2, as an important greenhouse gas [23], can be utilized to produce additional CO by reacting with carbon ($C + CO_2 = 2CO$) [20], thus realizing the resource utilization of CO_2, and the generated CO can be used to adjust the H_2/CO ratio of syngas or be utilized independently for other processes [24]. In addition, steam can attack the Al-O bond of the catalyst at high temperatures, which leads to the collapse of the catalyst framework [12]. This does not occur in CO_2 gasification. The regeneration of catalysts via gasification in CO_2 is an ideal process for the development of a sustainable economy. There must be a relationship between the effectiveness of the regeneration of catalysts and the catalyst's nature, types of carbon deposition, and so on [18]. Usually, the main forms of carbon are amorphous carbon, graphitic carbon, and filamentous carbon [25]. Thus, the carbon deposition characteristics of Co-based spinel oxides are worthy of consideration.

In this work, the carbon deposition on $CoAl_2O_4$ and strongly alkali-etched $CoAl_2O_4$ ($CoAl^vO_4$) spinel oxides from the CH_4 stage were investigated. We examine the impact of various factors (reaction time, calcination temperature of metal oxide, and reaction temperature) on the composition of carbon deposition. The compositions of carbon deposition are differentiated via fixed-bed in situ oxidation of CO_2 and air as well as CO_2/O_2-TG methods for eliminating carbon deposition. We demonstrate that reaction time, calcination temperature, and reaction temperature have no effect on the compositions of carbon deposition, and the material itself plays a crucial role in carbon deposition. This is mainly attributed to the introduction of Al^{3+} vacancies by alkali etching, which efficiently tunes the surface electronic structure in $CoAl_2O_4$.

2. Materials and Methods

2.1. Hydrothermal Synthesis of CoAl Spinel Oxides

The Co-Al spinel oxides were synthesized via a typical hydrothermal method followed by a thermal annealing process. The solution was formulated by mixing 0.01 mol $Co(NO_3)_2 \cdot 6H_2O$, $Al(NO_3)_2 \cdot 9H_2O$ (99.5%, Sinopharm, Shanghai, China) (Co/Al = 1/2 for $CoAl_2O_4$), and 0.05 mol urea into 60 mL of deionized water and stirring. The obtained solution was poured into a stainless-steel Teflonlined autoclave (100 mL) followed by reacting in a preheated oven at 120 °C for 12 h. The precipitate was washed with deionized water three times and then dried overnight at 60 °C.

Synthesis of $CoAl_2O_4$: The resulting solids powder was annealed in air at 750 °C for 2 h at a heating rate of 5 °C min^{-1}.

Synthesis of $CoAl^vO_4$ (v refers to cationic vacancies): An amount of 1 g of as-synthesized powder was soaked in 40 mL of 6.0 M NaOH at 60 °C for 60 min. The etched products were washed with deionized water several times and dried overnight at 60 °C. The resulting solids powder was annealed in air at 750 °C for 2 h at a heating rate of 5 °C min^{-1}.

The effect of different factors on the production of carbon deposition was examined, with materials designated according to the metal oxide–calcination temperature–reaction temperature. For instance, $CoAl_2O_4-750-700$ refers to the metal oxide $CoAl_2O_4$, which was calcined in air at 750 °C and then underwent reduction reactions at 700 °C. The parameters varied include the following:

(1) Reaction time: Reaction durations of 20 and 4 min were selected, with the corresponding samples labeled as $CoAl_2O_4-20$ and $CoAl_2O_4-4$, respectively.
(2) Calcination temperature of metal oxide: Temperatures of 700 and 800 °C were selected, and the corresponding samples were denoted as $CoAl_2O_4-700-700$, $CoAl^vO_4-700-700$ and $CoAl_2O_4-800-700$, $CoAl^vO_4-800-700$, respectively.
(3) Reaction temperature: Temperatures of 700 and 800 °C were selected, and the corresponding samples were denoted as $CoAl_2O_4-750-700$, $CoAl^vO_4-750-700$ and $CoAl_2O_4-750-800$, $CoAl^vO_4-750-800$, respectively.

2.2. Physical and Chemical Characterization

XRD (X-ray diffraction) patterns were acquired over a 2θ angular range of 20 to 90 degrees, employing a SmartLab 9 KW diffractometer (Rigaku, Tokyo, Japan) that utilized Cu Kα radiation source with a wavelength of λ = 1.5418 Å. Raman spectroscopy was collected on a HORIBA EVOLUTION Raman spectrometer (HORIBA, Kyoto, Japan) with a 532 nm laser excitation source. The morphologies of the samples were characterized by JEM-2100F transmission electron microscopy (TEM), Japan Electron Optics Laboratory Co., Ltd., Akishima, Tokyo, Japan. The carbon deposition on metal oxide was analyzed using thermogravimetric analysis (TGA). The sample (10 mg) was placed in an alumina crucible. The temperature was then raised from room temperature to 800 °C at a rate of 10 °C min^{-1} under air/CO_2 flow (50 mL min^{-1}). The sample remained heated at 800 °C for 10 min until no weight change was detected.

2.3. Reactivity Tests

The formation and elimination of carbon on metal oxide was carried out in a lab-scale fixed bed reactor. The 0.2 g samples (particle size range of 20–40 mesh) were placed in a quartz tube and heated to 700 °C with a heating rate of 10 °C min^{-1} under an N_2 atmosphere flowing at a rate of 160 mL min^{-1}. During the experiments, a changeover between 10 ± 0.5% CH_4/N_2, 10 ± 0.5% CO_2/N_2, and synthetic air gas streams was executed, maintaining the same flow rate of 160 mL min^{-1}. The product gases were analyzed by an online gas analyzer (MRU Vario Plus, Norwegian Subsea, Hovfaret 8, Oslo, Norway).

3. Results and Discussion

3.1. Effect of Different Factors on the Production of Carbon Deposition

3.1.1. Reaction Time

The compositions of carbon deposition formed during the methane conversion process are differentiated via subsequent in situ reaction of CO_2–air oxidation for eliminating carbon deposition.

At various methane reaction times, the gas product distribution during the reduction–oxidation reaction of $CoAl_2O_4$ with $CH_4-CO_2-O_2$ is shown in Figure 1. In the CO_2 oxidation stage, the trend of the CO_2 conversion into CO was observed on both $CoAl_2O_4-20$ and $CoAl_2O_4-4$. During the air oxidation process, a certain concentration of CO_2 was detected on $CoAl_2O_4-20$ and $CoAl_2O_4-4$ (Figure 1a,b), which suggests that some carbon deposition on $CoAl_2O_4$ is resistant to CO_2 oxidation and necessitate further oxidation in air.

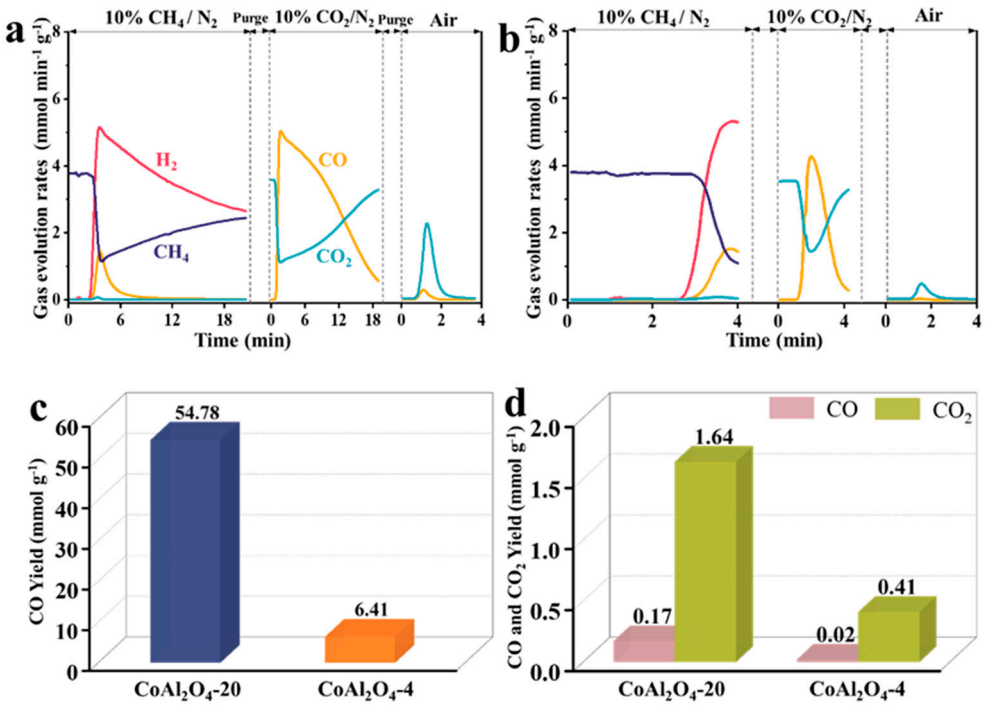

Figure 1. Gas evolution rates profiles in the reduction–oxidation process of CH_4-CO_2–air: (**a**) $CoAl_2O_4-20$; (**b**) $CoAl_2O_4-4$. (**c**) CO yield in the CO_2 oxidation stage; (**d**) CO and CO_2 yield in the air oxidation stage over $CoAl_2O_4-20$ and $CoAl_2O_4-4$.

The CO yield decreased from 54.78 mmol g^{-1} in $CoAl_2O_4-20$ to 6.41 mmol g^{-1} in $CoAl_2O_4-4$ during the CO_2 oxidation processes (Figure 1c), and similar declining trends were observed on $CoAl_2O_4-20$ and $CoAl_2O_4-4$ in air (Figure 1d), revealing that reaction time has a minimal effect on the compositions of carbon deposition on $CoAl_2O_4$, and has an effect on the amount of carbon.

3.1.2. Calcination Temperature of Metal Oxide

The crystal structures of $CoAl_2O_4$ and $CoAl^{V}O_4$ metal oxides calcined at different temperatures (700, 750, and 800 °C) were characterized and analyzed via XRD patterns, as illustrated in Figure 2.

For $CoAl_2O_4$, the diffraction peaks at 31.2, 36.7, 44.7, 55.5, 59.2, and 65.0° are assigned to (220), (311), (400), (422), (511), and (440) planes with d values of 0.29, 0.24, 0.20, 0.17, 0.160, and 0.14 nm, respectively. The diffraction peaks for $CoAl_2O_4-700$, $CoAl_2O_4-750$, and $CoAl_2O_4-800$ consistently maintain the same crystal structure after different calcination temperatures (Figure 2a). Similarly, the diffraction peaks in $CoAl^{V}O_4-700$, $CoAl^{V}O_4-750$, and $CoAl^{V}O_4-800$ agreed well with $CoAl_2O_4$, and no additional crystal phases were

observed (Figure 2b). Obviously, the XRD patterns of all the $CoAl^{v}O_4$ agreed well with $CoAl_2O_4$ (PDF #44-0160). These results demonstrate that calcination temperature does not affect the crystal structures of $CoAl_2O_4$ and $CoAl^{v}O_4$.

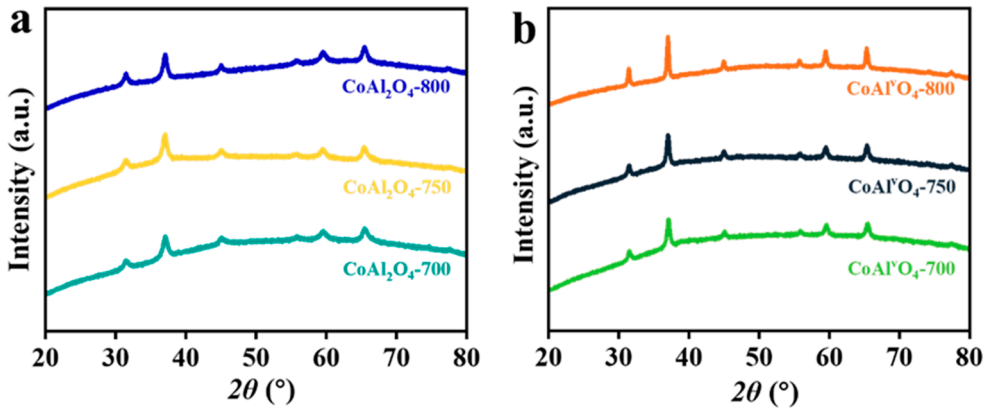

Figure 2. XRD patterns of (**a**) $CoAl_2O_4$ and (**b**) $CoAl^{v}O_4$.

At various calcination temperatures (700 and 800 °C) of metal oxides, the gas product distribution during the reduction–oxidation reaction of $CoAl_2O_4$ and $CoAl^{v}O_4$ with CH_4-CO_2–air is shown in Figure 3.

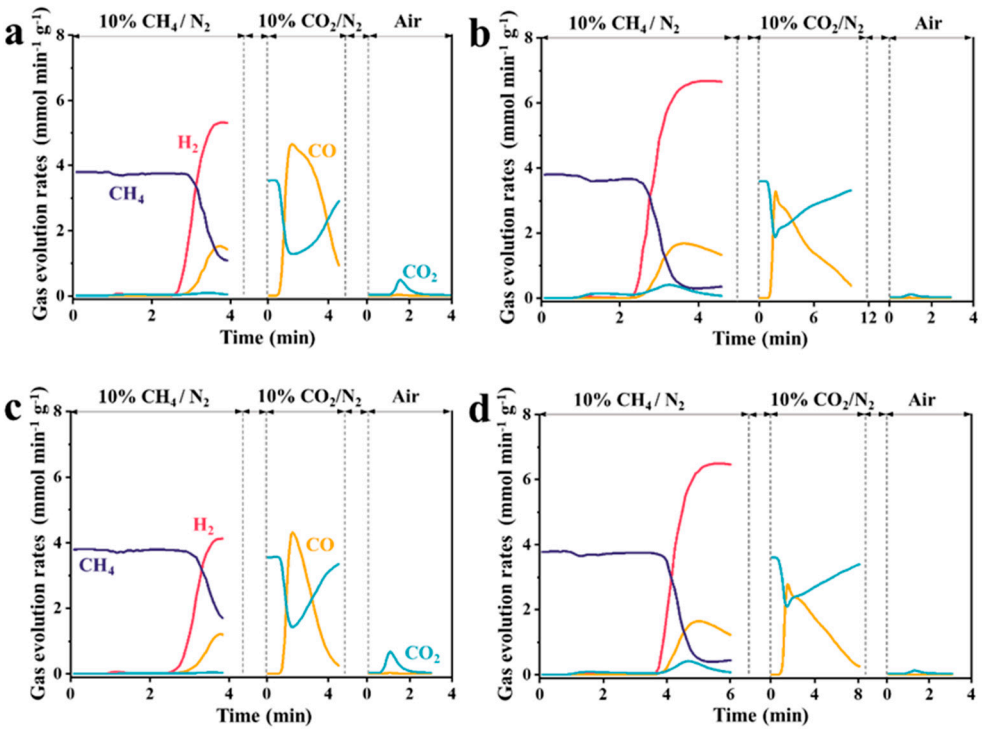

Figure 3. Gas evolution rates profiles in the reduction–oxidation process of CH_4-CO_2–air: (**a**) $CoAl_2O_4-700-700$; (**b**) $CoAl^{v}O_4-700-700$; (**c**) $CoAl_2O_4-800-700$; (**d**) $CoAl^{v}O_4-800-700$. Note: The dashed vertical lines indicate the separation between different the process.

The elimination process of carbon deposition on $CoAl_2O_4$ and $CoAl^{v}O_4$ metal oxides with calcination temperatures at 700 °C is shown in Figure 3a,b. In the CO_2 oxidation stage, similar trends were observed on both $CoAl_2O_4-700-700$ and $CoAl^{v}O_4-700-700$ metal oxides for the CO_2 conversion into CO. However, notable differences emerged in the air oxidation process. A certain concentration of CO_2 was detected on $CoAl_2O_4-700-700$, whereas $CoAl^{v}O_4-700-700$ exhibits an extremely low CO_2 concentration, suggesting that

carbon deposition on $CoAl^{V}O_4-700-700$ is almost completely removed during the CO_2 oxidation process. The trends observed for $CoAl_2O_4-800-700$ and $CoAl^{V}O_4-800-700$ agree with those recorded on $CoAl_2O_4-700-700$ and $CoAl^{V}O_4-700-700$ (Figure 3c,d).

The elimination process of carbon deposition on $CoAl_2O_4$ metal oxides with calcination temperatures at 700 and 800 °C is shown in Figure 3a,c. In the CO_2 oxidation stage, the phenomenon of the CO_2 conversion into CO was observed on both $CoAl_2O_4-700-700$ and $CoAl_2O_4-800-700$ metal oxides, and a certain concentration of CO_2 was detected on $CoAl_2O_4-700-700$ and $CoAl_2O_4-800-700$, showing that calcination temperature of metal oxide has a minor effect on carbon deposition. These results show that the calcination temperature of metal oxides has no effect on the compositions of carbon deposition, and the material itself plays a crucial role in influencing carbon deposition.

The CO and CO_2 yield during CO_2 and air oxidation processes are illustrated in Figure 4. During the CO_2 oxidation process, the CO yield increased from 12.46 mmol g^{-1} in $CoAl_2O_4-700-700$ to 14.25 mmol g^{-1} in $CoAl^{V}O_4-700-700$ (Figure 4a), which attributed to the superior methane conversion on $CoAl^{V}O_4-700-700$. In contrast to $CoAl_2O_4-700-700$, both CO and CO_2 yield on $CoAl^{V}O_4-700-700$ metal oxide decreases in the air oxidation process. The CO yield decreases from 0.02 mmol g^{-1} to 0.01 mmol g^{-1}, while the CO_2 yield decreases from 0.41 mmol g^{-1} to 0.14 mmol g^{-1} (Figure 4b). The trends in CO and CO_2 yield observed for $CoAl_2O_4-800-700$ and $CoAl^{V}O_4-800-700$ agree with those recorded on $CoAl_2O_4-700-700$ and $CoAl^{V}O_4-700-700$ (Figure 4c,d).

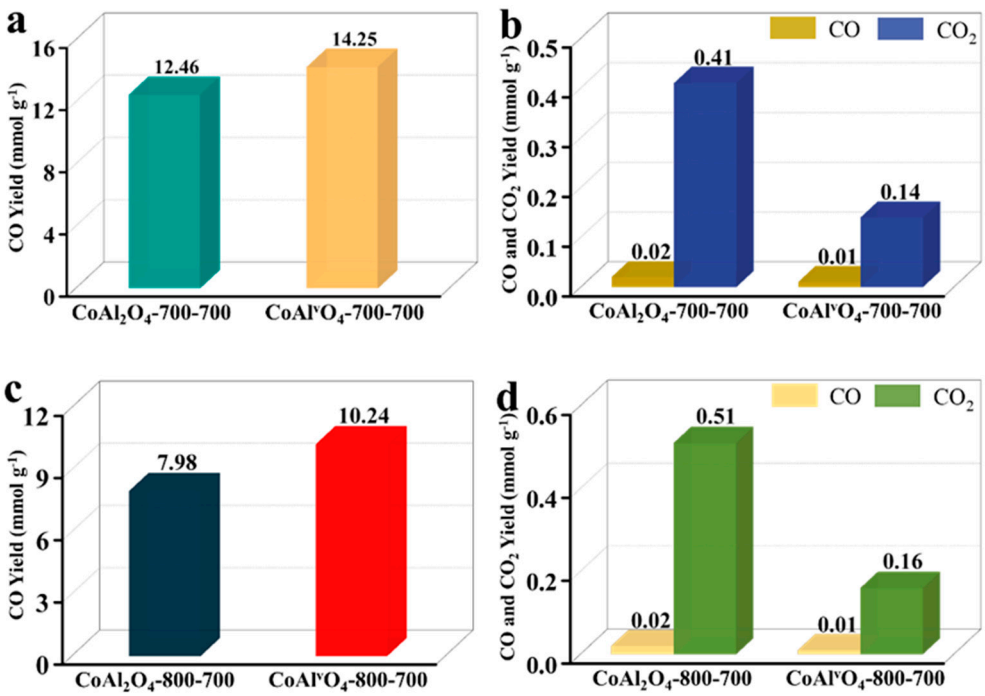

Figure 4. (**a**) CO yield in the CO_2 oxidation stage; (**b**) CO and CO_2 yield in the air oxidation stage over $CoAl_2O_4-700-700$ and $CoAl^{V}O_4-700-700$; (**c**) CO yield in the CO_2 oxidation stage; (**d**) CO and CO_2 yield in the air oxidation stage over $CoAl_2O_4-800-700$ and $CoAl^{V}O_4-800-700$.

For CO yield obtained at the different calcination temperatures (Figure 4a,c), as the calcination temperature increases from 700 to 800 °C, the CO yield decreased from 12.46 mmol g^{-1} in $CoAl_2O_4-700-700$ to 7.98 mmol g^{-1} in $CoAl_2O_4-800-700$. $CoAl^{V}O_4-700-700$ and $CoAl^{V}O_4-800-700$ showed the same trend. The possible reason is that the increase in calcination temperature leads to an increase in catalytic particle size, resulting in decreased activity of methane decomposition.

3.1.3. Reaction Temperature

At various reaction temperatures (700 and 800 °C), the gas product distribution during the reduction–oxidation reaction of $CoAl_2O_4$ and $CoAl^vO_4$ with CH_4-CO_2–air is shown in Figure 5.

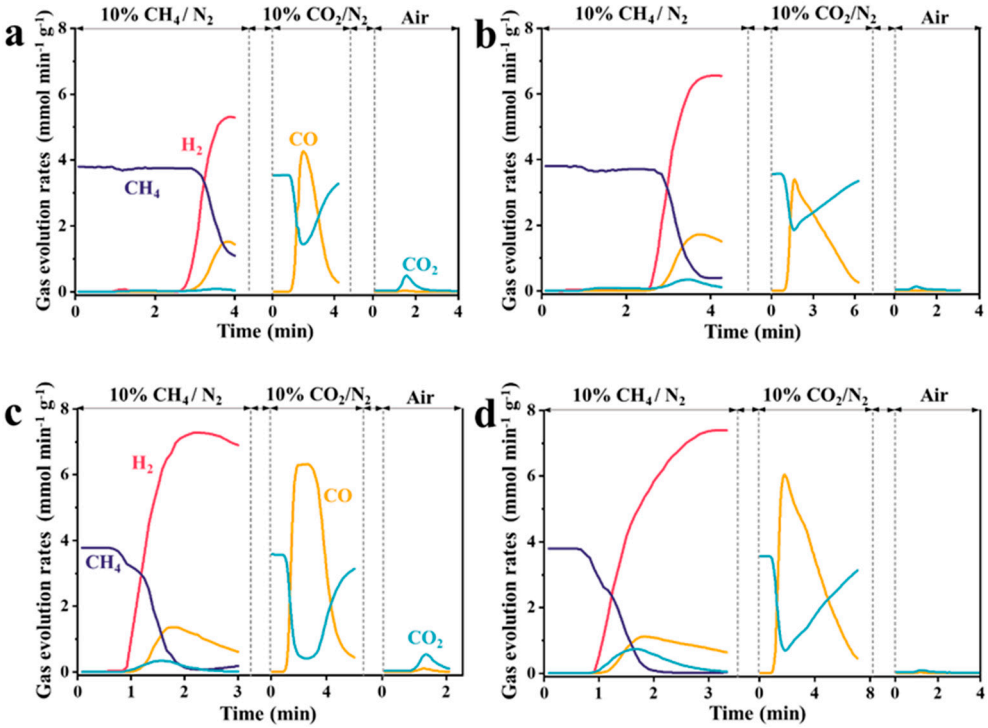

Figure 5. Gas evolution rates profiles in reduction–oxidation process of CH_4-CO_2–air: (**a**) $CoAl_2O_4-750-700$; (**b**) $CoAl^vO_4-750-700$; (**c**) $CoAl_2O_4-750-800$; (**d**) $CoAl^vO_4-750-800$.

The elimination process of carbon deposition on $CoAl_2O_4$ and $CoAl^vO_4$ metal oxides with reaction temperatures at 700 °C is shown in Figure 5a,b. In the CO_2 oxidation stage, similar trends were observed on both $CoAl_2O_4-750-700$ and $CoAl^vO_4-750-700$ for the C→CO. However, in the air oxidation process, a certain concentration of CO_2 was detected on $CoAl_2O_4-750-700$, whereas a low CO_2 concentration was exhibited on $CoAl^vO_4-750-700$, suggesting that carbon deposition on $CoAl^vO_4-750-700$ is almost completely removed during the CO_2 oxidation process. The trends observed for $CoAl_2O_4-750-800$ and $CoAl^vO_4-750-800$ agree with those recorded on $CoAl_2O_4-750-700$ and $CoAl^vO_4-750-700$ (Figure 5c,d), suggesting that the composition of carbon deposition remains unchanged despite variations in reaction temperature.

The CO and CO_2 yield during CO_2 and air oxidation processes are illustrated in Figure 6. During the CO_2 oxidation process, the CO yield increased from 6.4 mmol g^{-1} in $CoAl_2O_4-750-700$ to 8.92 mmol g^{-1} in $CoAl^vO_4-750-700$ (Figure 6a). In the air oxidation process, the CO yield decreases from 0.02 mmol g^{-1} in $CoAl_2O_4-750-700$ to 0.01 mmol g^{-1} in $CoAl^vO_4-750-700$, while the CO_2 yield decreases from 0.41 mmol g^{-1} to 0.1 mmol g^{-1} (Figure 6b). The trends in CO and CO_2 yield observed for $CoAl_2O_4-750-800$ and $CoAl^vO_4-750-800$ agree with those recorded on $CoAl_2O_4-750-700$ and $CoAl^vO_4-750-700$ (Figure 6c,d). However, $CoAl_2O_4-750-800$ and $CoAl^vO_4-750-800$, during the CO_2 oxidation process, exhibit CO yield than that of $CoAl_2O_4-750-700$ and $CoAl^vO_4-750-700$, indicating that an increase in reaction temperature leads to an increase carbon deposition from CH_4 conversion, resulting in higher CO yields during CO_2 conversion.

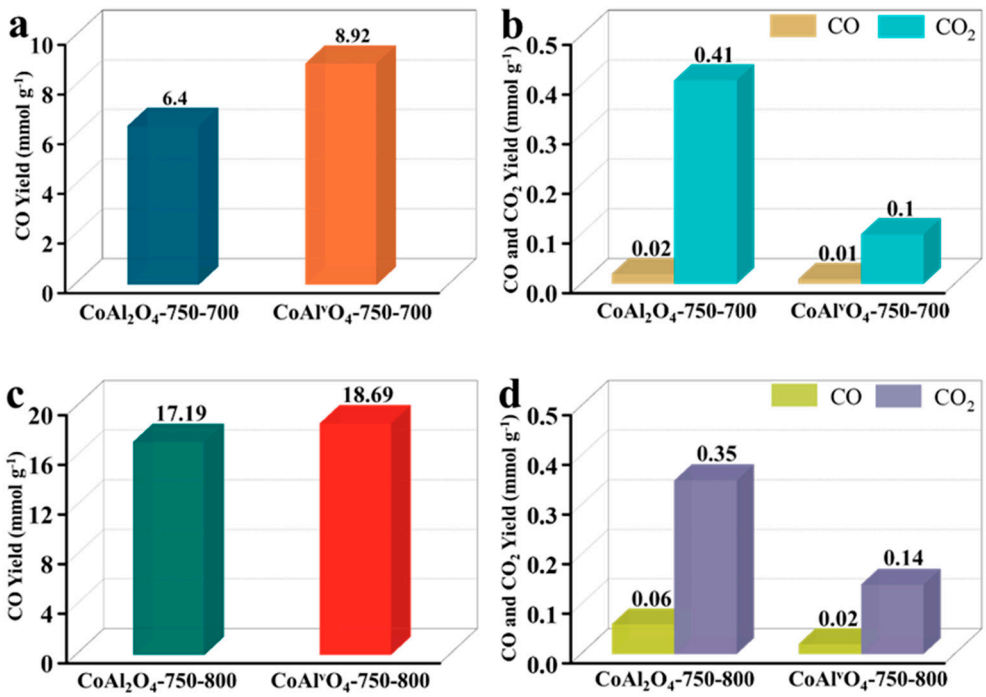

Figure 6. (**a**) CO yield in the CO_2 oxidation stage; (**b**) CO and CO_2 yield in the air oxidation stage over $CoAl_2O_4-750-700$ and $CoAl^vO_4-750-700$; (**c**) CO yield in the CO_2 oxidation stage; (**d**) CO and CO_2 yield in the air oxidation stage over $CoAl_2O_4-750-800$ and $CoAl^vO_4-750-800$.

3.2. Characterization of Carbon Deposition

3.2.1. Raman Analysis

To further confirm the elimination of carbon deposition in the oxidation process, Raman spectroscopy analyses were performed on $CoAl_2O_4-750-700$ and $CoAl^vO_4-750-700$ metal oxides under reduction–oxidation reaction with CH_4-CO_2–air, as shown in Figure 7. The Raman characteristic peaks appeared at ~1350 cm^{-1} corresponded to the D-band, and ~1580 cm^{-1} corresponded to the G-band, which represent lattice defects or amorphous carbon and highly ordered graphitic carbon structure, respectively [26].

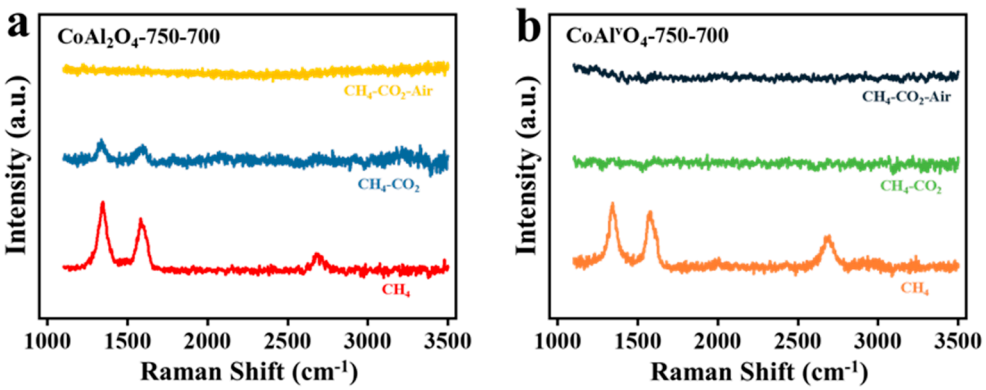

Figure 7. Raman patterns of (**a**) $CoAl_2O_4-750-700$ and (**b**) $CoAl^vO_4-750-700$ during different atmospheres.

The Raman spectra of $CoAl_2O_4-750-700$ and $CoAl^vO_4-750-700$ metal oxides show obvious differences during the oxidation process of CO_2 and air. For $CoAl_2O_4-750-700$, D and G peaks appear in the Raman spectrum during CH_4 conversion, but these peaks' intensity is significantly reduced during the CO_2 oxidation process. After O_2 oxidation, D and G peaks disappear (Figure 7a), indicating that carbon deposition cannot be com-

pletely removed in CO_2, which can be completely removed through oxidation in air. For $CoAl^{V}O_4-750-700$, it is worth noting that D and G peaks disappear in the Raman spectrum during the CO_2 oxidation process (Figure 7b).

The structure and composition of carbon species on $CoAl_2O_4$ and $CoAl^{V}O_4$ metal oxides were characterized using Raman spectroscopy, as shown in Figure 8. Raman spectroscopy is used to characterize the graphitization degree of carbon materials. The ID/IG ratio is used to assess the degree of graphitization of the carbon deposition on materials [27–29]. A lower ID/IG value indicates a higher degree of graphitization of the carbon species [26,27].

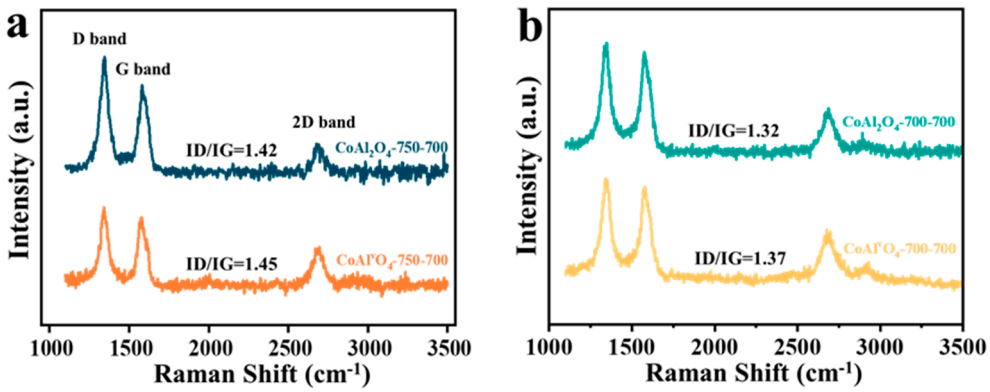

Figure 8. Raman patterns: (**a**) $CoAl_2O_4-750-700$ and $CoAl^{V}O_4-750-700$; (**b**) $CoAl_2O_4-700-700$ and $CoAl^{V}O_4-700-700$.

Raman spectroscopy showed ID/IG increased from 1.42 in $CoAl_2O_4-750-700$ to 1.45 in $CoAl^{V}O_4-750-700$ (Figure 8a), and similar trends were observed in $CoAl_2O_4-700-700$ and $CoAl^{V}O_4-700-700$ (Figure 8b), which indicates that the graphitization degree for $CoAl^{V}O_4$ is lower than that for $CoAl_2O_4$. The research indicates that a more disordered carbon structure exists in the carbon deposition with ID/IG values greater than 1 [27]. Consequently, the degree of graphitization of the carbon deposition decreases following treatment with strong alkali etching.

3.2.2. Microstructure Characterization

Some carbon nanotubes and carbon nano-onions have been observed on the surface of the $CoAl_2O_4-750-700$ and $CoAl^{V}O_4-750-700$ catalysts after CH_4 conversion at 700 °C, as shown in Figure 9.

The carbon nanotubes are straight and bamboo-like, with a hollow channel and metal particles on the end side (Figure 9a); the metal particles are observed to be trapped in a carbon nanotube cage (Figure 9b). The carbon nano onions (thick layer of graphite encapsulating metal particles) were observed on the $CoAl_2O_4-750-700$ surface (Figure 9b). In addition to carbon nanotubes and carbon nano-onions (Figure 9d), spiral carbon nanofibers were observed on the $CoAl^{V}O_4-750-700$ surface (Figure 9c). Therefore, the difference in carbon deposition behavior may be correlated to the difference in the material itself.

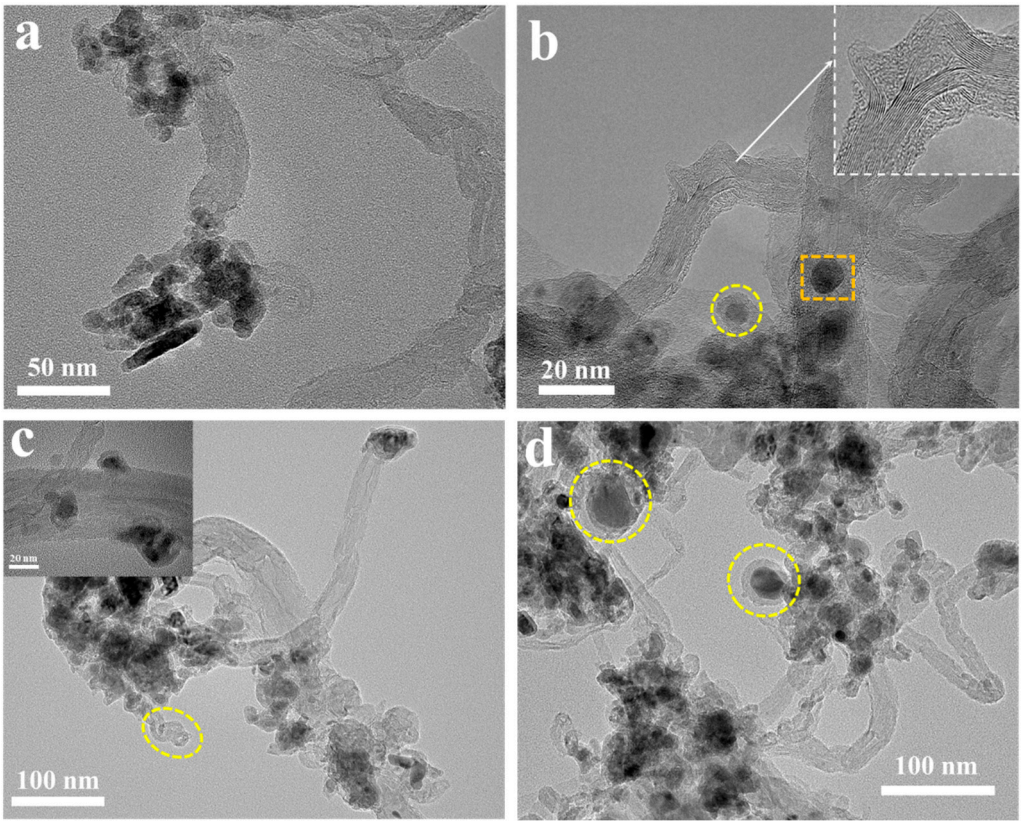

Figure 9. TEM images: (**a**,**b**) $CoAl_2O_4-750-700$; (**c**,**d**) $CoAl^VO_4-750-700$.

3.2.3. Thermogravimetric (TG) Analysis

To investigate the compositions of carbon deposition on $CoAl_2O_4$ and $CoAl^vO_4$ metal oxides, carbon deposition from the methane stage was analyzed using thermogravimetric analysis (TG) in O_2 and CO_2 [30].

The O_2 and CO_2-TGA analyses of $CoAl_2O_4$ and $CoAl^vO_4$ metal oxide are illustrated in Figure 10. The TGA curve could be divided into three stages of mass changes: (1) an initial slight weight loss(Yellow area) before 200 °C due to the elimination of absorbed water; (2) an increase in weight (White area) between approximately 200 and 300 °C, attributing to the oxidation of reduced $CoAl_2O_4$ and $CoAl^vO_4$ in the air; (3) a sharp decline (Purple area) in weight between approximately 300 and 450 °C, resulting from the removal of carbon deposition.

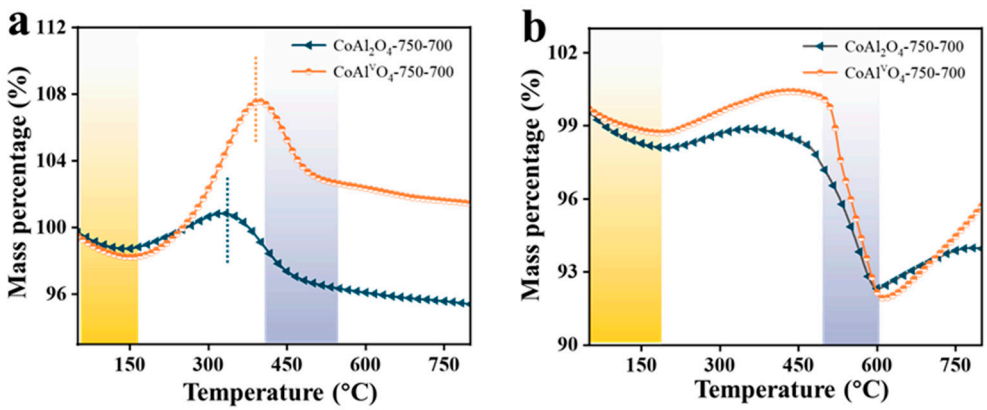

Figure 10. (**a**) O_2-TGA and (**b**) CO_2-TGA patterns of $CoAl_2O_4-750-700$ and $CoAl^VO_4-750-700$.

The weight-loss onset temperature of $CoAl^{v}O_4-750-700$ is especially higher than that of $CoAl_2O_4-750-700$ in O_2 oxidation (Figure 10a); however, this phenomenon is not obvious in CO_2 oxidation (Figure 10b), attributing to the prior restoration reaction of oxygen species in $CoAl^{v}O_4$ metal oxide before the carbon removal reaction.

The O_2 and CO_2-DTG analyses of $CoAl_2O_4$ and $CoAl^{v}O_4$ metal oxide are illustrated in Figure 11. In O_2-DTG curves, both $CoAl_2O_4$ and $CoAl^{v}O_4$ metal oxides exhibit a sharp derivative thermogravimetric (DTG) peak (Figure 11a). The maximum weight loss corresponding temperature of $CoAl^{v}O_4-750-700$ (447 °C) is higher than that of $CoAl_2O_4-750-700$ (399 °C).

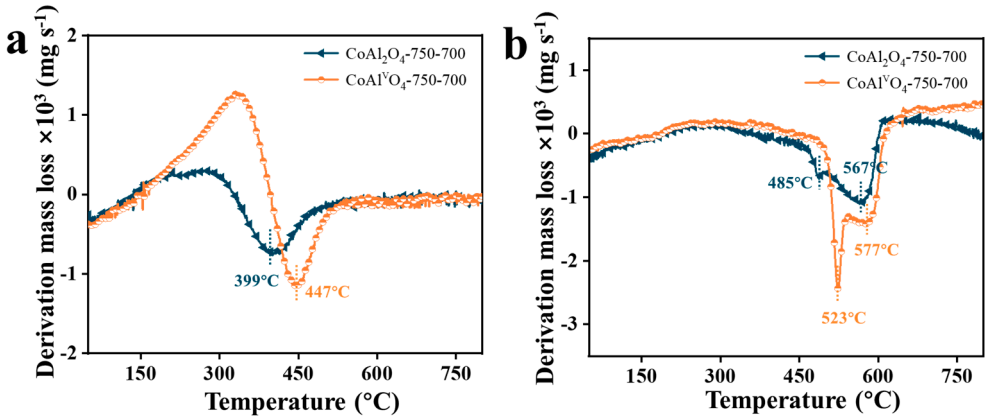

Figure 11. (**a**) O_2-DTG (**b**) CO_2-DTG patterns of $CoAl_2O_4-750-700$ and $CoAl^{v}O_4-750-700$.

According to the CO_2-DTG curve (Figure 11b), there were two obvious weightlessness stages of $CoAl_2O_4$ and $CoAl^{v}O_4$, which were located at ~500 and 570 °C, respectively. These results indicated the presence of two carbon compositions in $CoAl_2O_4$ and $CoAl^{v}O_4$. Normally, weight loss below 500 °C is caused by the oxidation of amorphous carbon and/or graphitic carbon fibers, whereas weight loss above 500 °C stems from the combustion of highly ordered graphitic carbon [28,31,32]. The research suggests that the carbon located close to the metal site is more easily removed, while carbon situated on the support requires higher temperatures to be eliminated [9]. For $CoAl_2O_4-750-700$, the temperature of the maximum rate of weight loss is 567 °C, while the temperature in $CoAl^{v}O_4-750-700$ is 523 °C, which indicates a higher content of graphitic carbon fibers in $CoAl^{v}O_4-750-700$. Therefore, $CoAl_2O_4$ by strong alkali etching only affects contents in different compositions of carbon deposition but does not affect compositions of carbon deposition. It is mainly attributed to the cation vacancies produced by alkali etching, which efficiently modulates the surface electronic structure of $CoAl_2O_4$ [33].

4. Conclusions

In this study, the carbon deposition on $CoAl_2O_4$ and strongly alkali-etched $CoAl_2O_4$ ($CoAl^{v}O_4$) from the CH_4 stage was investigated. We examine the impact of various factors (reaction time, calcination temperature of metal oxide, and reaction temperature) on the composition of carbon deposition. The compositions of carbon deposition are differentiated via fixed-bed in situ oxidation of CO_2 and air and CO_2/O_2-TG methods for eliminating carbon deposition. The main findings are presented below.

(1) The composition of carbon deposition over $CoAl_2O_4$ and $CoAl^{v}O_4$ depends on the material itself and reaction time; calcination temperature and reaction temperature do not affect the compositions of carbon deposition.
(2) In the CO_2 oxidation, similar trends were observed on both $CoAl_2O_4$ and $CoAl^{v}O_4$ for C→CO. However, a certain concentration of CO_2 was detected on $CoAl_2O_4$ in the air oxidation process, whereas $CoAl^{v}O_4$ exhibits an extremely low CO_2 concentration,

suggesting that carbon deposition on $CoAl^vO_4$ is almost completely removed during the CO_2 oxidation process. This trend is also confirmed by Raman spectra.

(3) Raman spectroscopy showed that ID/IG in $CoAl^vO_4$ is higher than that of $CoAl_2O_4$, indicating the decrease in the degree of graphitization of the carbon deposition on $CoAl^vO_4$. Thermogravimetric analysis showed that the strong alkali etching in $CoAl_2O_4$ only affects contents in different types of carbon deposition. It is mainly attributed to the cation vacancies produced by alkali etching, which efficiently modulates the surface electronic structure of $CoAl_2O_4$, thus resulting in differences in carbon deposition on $CoAl^vO_4$ surface compared to $CoAl_2O_4$.

Notably, CO_2 can be utilized to produce CO by eliminating carbon deposition on the CoAl spinel oxides, which realizes the utilization of CO_2, and the generated CO can be used to adjust the H_2/CO ratio of syngas or be utilized independently for other processes. Meanwhile, carbon deposition on $CoAl^vO_4$ can be removed by oxidation with CO_2, avoiding hot spots caused by the oxidation with air, thereby reducing damage to the catalyst.

Author Contributions: X.Z.: Conceptualization, data curation, investigation, formal analysis, writing—original draft and review and editing. J.W.: Conceptualization, writing—review and editing. Z.S.: Funding acquisition, conceptualization, formal analysis, writing—review and editing. Y.P.: Formal analysis, writing—review and editing. All authors have read and agreed to the published version of the manuscript.

Funding: This work was supported by the National Natural Science Foundation of China (52276203), the Natural Science Foundation of Shandong Province (ZR2021ME090, ZR2022QB079), and the Postdoctoral Innovation Project of Shandong Province (202102005).

Institutional Review Board Statement: Not applicable.

Informed Consent Statement: Not applicable.

Data Availability Statement: The data presented in this study are available upon request from the corresponding author.

Conflicts of Interest: The authors declare no conflict of interest.

References

1. Serbin, S.; Radchenko, M.; Pavlenko, A.; Burunsuz, K.; Radchenko, A.; Chen, D. Improving Ecological Efficiency of Gas Turbine Power System by Combusting Hydrogen and Hydrogen-Natural Gas Mixtures. *Energies* **2023**, *16*, 3618. [CrossRef]
2. Zhao, X.; Zhou, H.; Sikarwar, V.S.; Zhao, M.; Park, A.H.A.; Fennell, P.S.; Shen, L.H.; Fan, L.S. Biomass-based chemical looping technologies: The good, the bad and the future. *Energy Environ. Sci.* **2017**, *10*, 1885–1910. [CrossRef]
3. Lee, C.T.; Hashim, H.; Ho, C.S.; Fan, Y.V.; Klemeš, J.J. Sustaining the low-carbon emission development in Asia and beyond: Sustainable energy, water, transportation and low-carbon emission technology. *J. Clean. Prod.* **2017**, *146*, 1–13. [CrossRef]
4. Sarathy, S.M.; Nagaraja, S.S.; Singh, E.; Cenker, E.; Amer, A. Review of life cycle assessments (LCA) for mobility powertrains. *Transp. Eng.* **2022**, *10*, 100148. [CrossRef]
5. Wu, Y.; Chen, A.; Xiao, H.; Jano-Ito, M.; Alnaeli, M.; Alnajideen, M.; Mashruk, S.; Valera-Medina, A. Emission reduction and cost-benefit analysis of the use of ammonia and green hydrogen as fuel for marine applications. *Green Energy Resour.* **2023**, *1*, 100046. [CrossRef]
6. Galvita, V.V.; Poelman, H.; Detavernier, C.; Marin, G.B. Catalyst-assisted chemical looping for CO_2 conversion to CO. *Appl. Catal. B Environ.* **2015**, *164*, 184–191. [CrossRef]
7. Chen, J.; Zhao, K.; Zhao, Z.; He, F.; Huang, Z.; Wei, G.; Xia, C. Reaction schemes of barium ferrite in biomass chemical looping gasification for hydrogen-enriched syngas generation via an outer-inner looping redox reaction mechanism. *Energy Convers. Manag.* **2019**, *189*, 81–90. [CrossRef]
8. Omoniyi, O.A.; Dupont, V. Chemical looping steam reforming of acetic acid in a packed bed reactor. *Appl. Catal. B Environ.* **2018**, *226*, 258–268. [CrossRef]
9. Jiao, F.; Li, J.; Pan, X.; Xiao, J.; Li, H.; Ma, H.; Wei, M.; Pan, Y.; Zhou, Z.; Li, M.; et al. Selective conversion of syngas to light olefins. *Science* **2016**, *351*, 1065–1068. [CrossRef]
10. Shen, Q.; Huang, F.; Tian, M.; Zhu, Y.; Li, L.; Wang, J.; Wang, X. Effect of Regeneration Period on the Selectivity of Synthesis Gas of Ba-Hexaaluminates in Chemical Looping Partial Oxidation of Methane. *ACS Catal.* **2019**, *9*, 722–731. [CrossRef]

11. Ashok, J.; Kathiraser, Y.; Ang, M.L.; Kawi, S. Bi-functional hydrotalcite-derived NiO–CaO–Al_2O_3 catalysts for steam reforming of biomass and/or tar model compound at low steam-to-carbon conditions. *Appl. Catal. B Environ.* **2015**, *172–173*, 116–128. [CrossRef]
12. Zhou, J.; Zhao, J.; Zhang, J.; Zhang, T.; Ye, M.; Liu, Z. Regeneration of catalysts deactivated by coke deposition: A review. *Chin. J. Catal.* **2020**, *41*, 1048–1061. [CrossRef]
13. Guisnet, M.; Magnoux, P. Organic chemistry of coke formation. *Appl. Catal. A Gen.* **2001**, *212*, 83–96. [CrossRef]
14. Zhu, M.; Chen, S.; Ma, S.; Xiang, W. Carbon formation on iron-based oxygen carriers during CH_4 reduction period in Chemical Looping Hydrogen Generation process. *Chem. Eng. J.* **2017**, *325*, 322–331. [CrossRef]
15. Huang, J.; Yan, Y.; Saqline, S.; Liu, W.; Liu, B. High performance Ni catalysts prepared by freeze drying for efficient dry reforming of methane. *Appl. Catal. B Environ.* **2020**, *275*, 119109. [CrossRef]
16. Yu, Q.; Liu, C.; Li, X.; Wang, C.; Wang, X.; Cao, H.; Zhao, M.; Wu, G.; Su, W.; Ma, T.; et al. N-doping activated defective Co_3O_4 as an efficient catalyst for low-temperature methane oxidation. *Appl. Catal. B Environ.* **2020**, *269*, 118757. [CrossRef]
17. Kim, Y.; Kim, H.S.; Kang, D.; Kim, M.; Lee, J.W. Enhanced redox performance of $LaFeO_3$ perovskite through in-situ exsolution of iridium nanoparticles for chemical looping steam methane reforming. *Chem. Eng. J.* **2023**, *468*, 143662. [CrossRef]
18. Duy, N.P.H.; Phuong, N.N.; Ngoc, L.T.B.; Tri, N.; Nguyen, H.-H.T.; Vo, D.-V.N.; Phuong, P.T.T. Deactivation and in-situ regeneration of Dy-doped Ni/SiO_2 catalyst in CO_2 reforming of methanol. *Int. J. Hydrogen Energy* **2023**, *48*, 21224–21239.
19. Fan, Z.; Weng, W.; Zhou, J.; Gu, D.; Xiao, W. Catalytic decomposition of methane to produce hydrogen: A review. *J. Energy Chem.* **2021**, *58*, 415–430. [CrossRef]
20. Lim, H.S.; Kang, D.; Lee, J.W. Phase transition of Fe_2O_3-NiO to $NiFe_2O_4$ in perovskite catalytic particles for enhanced methane chemical looping reforming-decomposition with CO_2 conversion. *Appl. Catal. B Environ.* **2017**, *202*, 175–183. [CrossRef]
21. Mikkelsen, M.; Jørgensen, M.; Krebs, F.C. The teraton challenge. A review of fixation and transformation of carbon dioxide. *Energy Environ. Sci.* **2010**, *3*, 43–81. [CrossRef]
22. Kim, Y.; Lim, H.S.; Kim, H.S.; Lee, M.; Lee, J.W.; Kang, D. Carbon dioxide splitting and hydrogen production using a chemical looping concept: A review. *J. CO_2 Util.* **2022**, *63*, 102139.
23. Wang, L.; Qi, Y.; Yang, Z.; Wu, H.; Liu, J.; Tang, Y.; Wang, F. Pt nanoparticles supported $LaCoO_3$ as highly efficient catalysts for photo-thermal catalytic CO_2 methanation. *Green Energy Resour.* **2023**, *1*, 100036. [CrossRef]
24. Zhang, X.; Wang, J.; Song, Z.; Zhao, X.; Sun, J.; Mao, Y.; Wang, W. Co_3O_4-CeO_2 for enhanced syngas by low-temperature methane conversion with CO_2 utilization via a catalytic chemical looping process. *Fuel Process. Technol.* **2023**, *245*, 107741. [CrossRef]
25. Zhu, M.; Song, Y.; Chen, S.; Li, M.; Zhang, L.; Xiang, W. Chemical looping dry reforming of methane with hydrogen generation on Fe_2O_3/Al_2O_3 oxygen carrier. *Chem. Eng. J.* **2019**, *368*, 812–823. [CrossRef]
26. Kang, D.; Lee, J.W. Enhanced methane decomposition over nickel–carbon–B_2O_3 core–shell catalysts derived from carbon dioxide. *Appl. Catal. B Environ.* **2016**, *186*, 41–55. [CrossRef]
27. Mo, W.; Ma, F.; Ma, Y.; Fan, X. The optimization of Ni–Al_2O_3 catalyst with the addition of La_2O_3 for CO_2–CH_4 reforming to produce syngas. *Int. J. Hydrogen Energy* **2019**, *44*, 24510–24524. [CrossRef]
28. Liu, C.; Chen, D.; Cao, Y.; Zhang, T.; Mao, Y.; Wang, W.; Wang, Z.; Kawi, S. Catalytic steam reforming of in-situ tar from rice husk over MCM-41 supported $LaNiO_3$ to produce hydrogen rich syngas. *Renew. Energy* **2020**, *161*, 408–418. [CrossRef]
29. Sastre, D.; Serrano, D.P.; Pizarro, P.; Coronado, J.M. Chemical insights on the activity of $La_{1-x}Sr_xFeO_3$ perovskites for chemical looping reforming of methane coupled with CO_2-splitting. *J. CO_2 Util.* **2019**, *31*, 16–26.
30. Gao, R.; Li, X.; Wang, Z.; Liu, Y.; Sun, J.; Zhu, Y.; Yao, S. Reaction regeneration cycle of Mo/HZSM-5 catalyst in methane dehydroaromatization with the addition of oxygen-containing components. *Appl. Catal. A Gen.* **2022**, *647*, 118916. [CrossRef]
31. Qingli, X.; Zhengdong, Z.; Kai, H.; Shanzhi, X.; Chuang, M.; Chenge, C.; Huan, Y.; Yang, Y.; Yongjie, Y. Ni supported on MgO modified attapulgite as catalysts for hydrogen production from glycerol steam reforming. *Int. J. Hydrogen Energy* **2021**, *46*, 27380–27393. [CrossRef]
32. Wang, Y.; Chen, M.; Yang, Z.; Liang, T.; Liu, S.; Zhou, Z.; Li, X. Bimetallic Ni-M (M=Co, Cu and Zn) supported on attapulgite as catalysts for hydrogen production from glycerol steam reforming. *Appl. Catal. A Gen.* **2018**, *550*, 214–227. [CrossRef]
33. Wang, H.; Zeng, Y.; Mao, H.; Huang, H.; Hu, Y. Alkali Etching Induced CoAl-Layered Double Oxides with Regulatable Cation and Oxygen Vacancy Defects to Promote the Photothermal Degradation of Methanol. *ChemNanoMat* **2022**, *8*, e202200263. [CrossRef]